

SCIENCE CHINA Earth Sciences

Decision Letter (SCES-2019-0099,R2)**From:** wjj@scichina.org**To:** xhuang@whu.edu.cn**CC:****Subject:** SCIENCE CHINA Earth Sciences - Decision on Manuscript ID SCES-2019-0099,R2**Body:** 08-Nov-2019

Dear Prof. Huang:

It is a pleasure to accept your manuscript entitled "Advances in Urban Information Extraction From High-Resolution Remote Sensing Imagery" in its current form for publication in the SCIENCE CHINA Earth Sciences.


Thank you for your fine contribution. On behalf of the Editors of the SCIENCE CHINA Earth Sciences, we look forward to your continued contributions to the Journal.

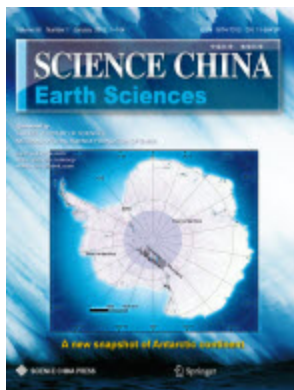
Sincerely,
Dr. JianJing Wei
Editor, SCIENCE CHINA Earth Sciences
wjj@scichina.org

Reviewer(s)' Comments to Author:

Editor(s)' Comments to Author:

Editor
Comments to the Author:
(There are no comments.)

Date Sent: 08-Nov-2019 Close Window



Advances in Urban Information Extraction From High-Resolution Remote Sensing Imagery

Journal:	<i>SCIENCE CHINA Earth Sciences</i>
Manuscript ID	SCES-2019-0099.R2
Manuscript Type:	Review
Date Submitted by the Author:	05-Nov-2019
Complete List of Authors:	Gong, Jianya; Wuhan University, School of Remote Sensing and Information Engineering Liu, Chun; Wuhan University, State Key Laboratory of Information Engineering in Surveying, Mapping and Remote Sensing Huang, Xin; Wuhan University, School of Remote Sensing and Information Engineering; Wuhan University, State Key Laboratory of Information Engineering in Surveying, Mapping and Remote Sensing
Keywords:	High-resolution, Urban remote sensing, Feature extraction, Land use/land cover classification, Change detection
Speciality:	Earth observation, Remote sensing
<p>Note: The following files were submitted by the author for peer review, but cannot be converted to PDF. You must view these files (e.g. movies) online.</p>	
<p>图片文件.zip</p>	

SCHOLARONE™
Manuscripts

Advances in urban information extraction from high-resolution remote sensing imagery

Jianya GONG¹, Chun LIU^{2*}, Xin HUANG^{1,2*}

¹ School of Remote Sensing and Information Engineering, Wuhan University, Wuhan 430079, China;

² State Key Laboratory of Information Engineering in Surveying, Mapping and Remote Sensing, Wuhan University, Wuhan 430079, China

* Corresponding authors (email: liuchun919@whu.edu.cn; xhuang@whu.edu.cn)

Abstract Urban is one of the hottest research topics in the field of remote sensing. With the accumulation of high-resolution (HR) remote sensing data and emerging of new satellite sensors, HR observation of urban areas has become increasingly possible, which provides us with more elaborate urban information. However, the strong heterogeneity in the spectral and spatial domain of HR imagery brings great challenges to urban remote sensing. In recent years, numerous approaches were proposed to deal with HR image interpretation over complex urban scenes, including a series of features from low level to high level, as well as state-of-the-art methods depicting not only the urban extent, but also the intra-urban variations. In this paper, we aim to summarize the major advances in HR urban remote sensing from the aspects of feature representation and information extraction. Moreover, the future trends are discussed from the perspectives of methodology, urban structure and pattern characterization, big data challenge, and global mapping.

Key words High-resolution, Urban remote sensing, Feature extraction, Land use/land cover classification, Change detection

1. Introduction

Urban is the core of human habitation, and is also the most active region for social and economic activities. According to the United Nations, the proportion of global urban residents increased from 30% to 55% between 1950 and 2018, and it is predicted to reach 68% by 2050. About 90% of this growth will take place in Africa and Asia, where the level of urbanization is relatively low at present (United Nations, 2018). Although cities account for only a small share (< 3%) of the Earth's land surface, they significantly impact both natural and human systems from regional to global scales (Gamba and Herold, 2009). The rapid urban expansion is accompanied by the disappearance of the

31 surrounding cultivated land, forest, and water areas, which brings a series of resource, environmental,
32 and ecological problems (Gong et al., 2012; Pesaresi et al., 2015).

33 Table 1 Typical high-resolution satellites (PAN: panchromatic band, MS: multispectral bands)

Satellite	Launch time	Country	Bands and spatial resolution	Swath width	Revisit cycle
IKONOS-2	1999-09	America	a) PAN: nadir 0.82 m; off-nadir 1 m b) 4 MS (blue, green, red, near-infrared): nadir 3.20 m; off-nadir 4 m	11.3 km	3 days
QuickBird-2	2001-10	America	a) PAN: 0.61 m b) 4 MS (blue, green, red, near-infrared): 2.40 m	16.5 km	1–3.5 days
Cartosat-1	2005-05	India	PAN: 2.50 m	26 km	5 days
Beijing-1	2005-10	China	a) PAN: 4 m b) 3 MS (green, red, near-infrared): 32 m	a) PAN: 24 km b) MS: 600 km	3–7 days
ALOS-PRISM	2006-01	Japan	PAN: 2.50 m	35 km	5 days
EROS-B	2006-04	Israel	PAN: 0.70 m	7 km	2–10 days
Cartosat-2	2A: 2007-01 2B: 2008-04	India	PAN: 0.80 m	9.6 km	4 days
TianHui-1	01: 2010-08 02: 2012-05 03: 2015-10	China	a) PAN: 5 m b) HR PAN: 2 m c) 4 MS (blue, green, red, near-infrared): 10 m	60 km	1 days
ZiYuan-3	01: 2012-01 02: 2016-05	China	a) PAN: nadir 2.10 m; off-nadir 3.50 m (01), 2.50 m (02) b) 4 MS (blue, green, red, near-infrared): 5.80 m	50 km	5 days
SPOT-6/7	SPOT-6: 2012-09 SPOT-7: 2014-06	France	a) PAN: 1.50 m b) 4 MS (blue, green, red, near-infrared): 6 m	60 km	1–5 days
GaoFen-1	2013-04	China	a) PAN: 2 m b) 4 MS (blue, green, red, near-infrared): 8 m and 16 m	68 km with two HR cameras and 830 km with four wide-field imager	≤ 4 days
WorldView-3	2014-08	America	a) PAN: nadir 0.31 m; off-nadir 0.34 m b) 8 MS (red, red edge, coastal, blue, green, yellow, near-infrared1, near-infrared2): nadir 1.24 m; off-nadir 1.38 m c) 8 short-wave infrared: nadir 3.70 m; off-nadir 4.10 m d) 12 CAVIS: nadir 30 m	13.1 km	1–4.5 days
GaoFen-2	2014-08	China	a) PAN: 0.81 m b) 4 MS (blue, green, red, near-infrared): 3.24 m	45 km	≤ 4 days
SuperView-1	01/02: 2016-12 03/04: 2018-01	China	a) PAN: 0.5 m b) 4 MS (blue, green, red, near-infrared): 2 m	12 km	1 day with 4 satellites

1
2
3
4 34 Urban remote sensing, as one of the most important branches in the field of remote sensing,
5
6 35 mainly refers to the use of remote sensing technologies to obtain urban information for monitoring,
7
8 36 understanding, and predicting the various urban phenomena, and to support decision making in urban
9
10 37 planning, disaster response, and sustainable development. In recent decades, with the considerable
11
12 38 developments of aerospace technology, a number of high-resolution (HR) satellites have been launched
13
14 39 (Table 1). The spatial resolution of civilian/commercial remote sensing imagery has achieved meter
15
16 40 and even sub-meter levels. Through different observation modes, such as satellite networking and
17
18 41 along-track or cross-track imaging, many of the HR satellites (e.g., QuickBird,
19
20 42 Cartosat-1/2, ZiYuan-3 (ZY-3), and SPOT-6/7) have the ability of stereo mapping. HR imagery can
21
22 43 substantially reduce the phenomenon of mixed-pixels with enhanced spatial details of ground objects.
23
24 44 Meanwhile, multi-angle observation is able to provide three-dimensional (3D) information, which
25
26 45 increase the dimension of urban information extraction (Huang et al., 2018b; Huang et al., 2017a; Peng
27
28 46 et al., 2017). Nevertheless, the problems such as spectral heterogeneity, shadow, occlusion, and
29
30 47 disparity are distinct in HR images, especially in urban settings, which present new challenges for
31
32 48 urban information extraction. Hence the traditional methods that rely purely upon spectral
33
34 49 characteristics may be insufficient to tackle these problems (Huang et al., 2007b; Peng et al., 2015).

35 50 Compared to natural surfaces, urban areas have more distinct textural and structural variations in
36
37 51 HR images, due to the inclusion of artificial surfaces such as buildings and roads. Given these
38
39 52 characteristics, many studies have incorporated both spectral and spatial features to improve the
40
41 53 interpretation accuracy of HR images over urban areas. In this paper, we mainly focus on introducing
42
43 54 state-of-the-art urban features, as well as urban information extraction based on HR remote sensing
44
45 55 imagery from the following aspects: 1) detection of urban targets, e.g., buildings, roads, impervious
46
47 56 surfaces, urban vegetation, and water bodies; 2) classification of urban land use/land cover, such as
48
49 57 urban scene recognition and functional zone mapping; 3) change detection, i.e., dynamic monitoring of
50
51 58 the urban landscape; and 4) urban ecology and climate, e.g., urban heat island and ecosystem service
52
53 59 assessment. A framework of HR urban remote sensing is illustrated in Figure 1. Finally, the future
54
55 60 research trends in HR urban remote sensing are prospected.

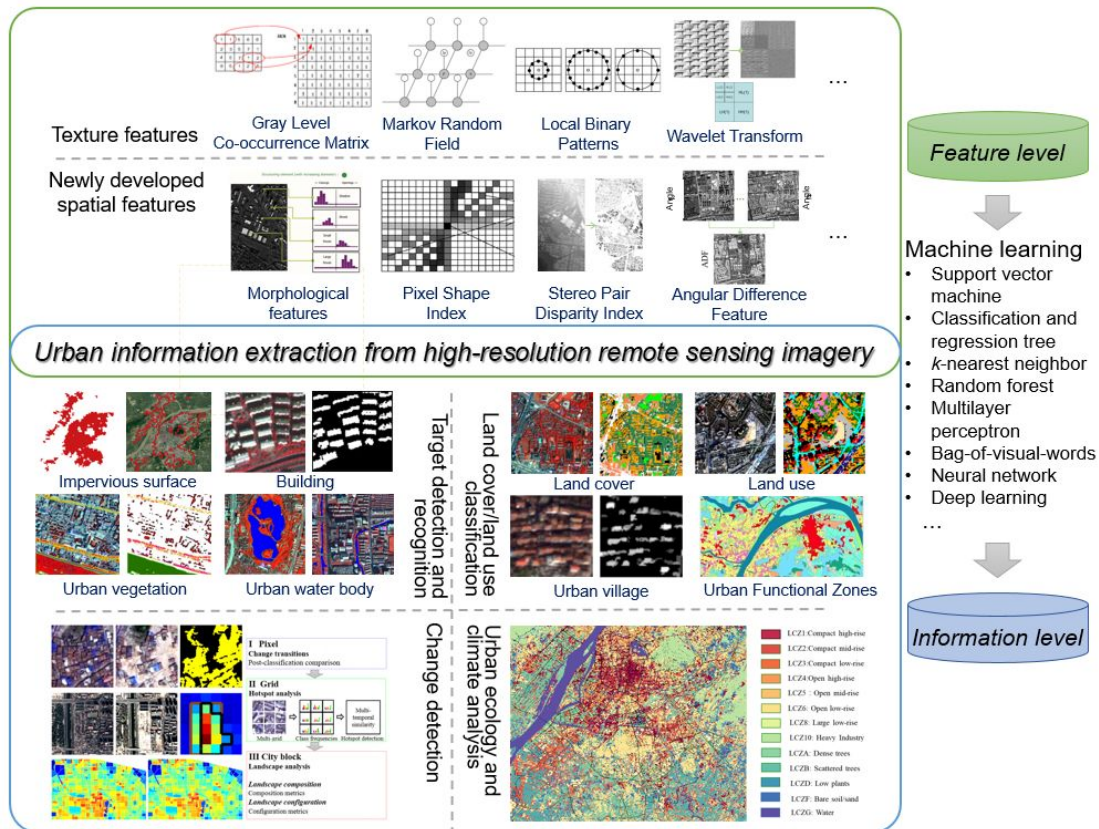


Figure 1 The framework of urban information extraction from high-resolution remote sensing imagery.

2. Urban feature extraction from high-resolution remote sensing imagery

The widely used texture features are calculated based mainly on statistical and spatial-frequency domain analysis, e.g., the gray-level co-occurrence matrix (Haralick and Shanmugam, 1973), wavelet transform (Mallat, 1989), and local binary patterns (Ojala et al., 1996). Moreover, a series of planar and stereo features, e.g., the pixel shape index (Zhang et al., 2006), PanTex (Pesaresi et al., 2008), morphological features (Pesaresi and Benediktsson, 2001), and angular features (Huang et al., 2018b), were specially designed for HR images to characterize urban environments. In addition, the recent advances in the domain of machine learning (e.g., deep learning) show strong abilities for high-level feature representation, which show promising avenues to address complex HR urban remote sensing problems (Zhu et al., 2017).

2.1 Textural features

2.2.1 Gray-level co-occurrence matrix

The gray-level co-occurrence matrix (GLCM) is a classical statistical texture extraction method. A series of statistical measures, e.g., homogeneity (HOM), contrast (CON), angular second moment

1
2
3
4 78 (ASM), and entropy (ENT), were defined to characterize the co-occurrence matrix to reflect the
5
6 79 grayscale changes and textural features of the image (Haralick and Shanmugam, 1973). For HR urban
7
8 80 remote sensing, Puissant et al. (2005) and Su et al. (2008) combined the spectral information and the
9
10 81 GLCM textures of HR images for urban classification, demonstrating the effectiveness of the GLCM
11
12 82 features to complement the spectral information. To overcome the influence of the “window effect” of
13
14 83 the spatial features, Huang et al. (2007a) presented an adaptive multi-scale feature fusion method,
15
16 84 which automatically selects the best window size according to the spectral and boundary information,
17
18 85 and integrates the multi-scale features to extract ground objects of different sizes. Standard GLCM
19
20 86 textures are calculated based on one band, therefore the first principal component or one of the bands is
21
22 87 widely employed when dealing with multi/hyperspectral imagery (Pacifici et al., 2009). In order to
23
24 88 exploit all the useful information, Huang et al. (2014b) proposed a multichannel GLCM calculation
25
26 89 method via image coding techniques to extract the synthesized texture features from
27
28 90 multi/hyperspectral bands.

29 91 *2.1.2 Wavelet transform*

30
31 92 Wavelet transform (WT), which was developed in the 1980s (Mallat, 1989), has been widely applied in
32
33 93 texture analysis. The standard WT is based on orthogonal wavelet basis, aiming to obtain the
34
35 94 multi-scale information, and extract the high- and low-frequency features of each layer. Myint et al.
36
37 95 (2004) compared the WT, GLCM, spatial autocorrelation, and fractal approaches for extracting urban
38
39 96 textures from HR images, suggesting that WT was more effective than the other methods. Ouma et al.
40
41 97 (2006) constructed multi-scale textural features through WT, and combined them with the spectral
42
43 98 features to extract urban trees from QuickBird imagery. The 3D-WT processes the multispectral
44
45 99 imagery as a cube and extracts spectral and spatial information simultaneously, hence it provides a
46
47 100 more adequate feature representation for multi/hyperspectral images (Guo et al., 2014; Huang and
48
49 101 Zhang, 2012b; Li et al., 2017a; Qian et al., 2013; Yoo et al., 2009). For instance, Yoo et al. (2009)
50
51 102 constructed the urban complexity index (UCI) based on 3D-WT, in order to discriminate complex
52
53 103 urban areas and natural surfaces. Accordingly, Huang and Zhang (2012b) proposed the multi-scale UCI
54
55 104 (M-UCI) to further enhance the performance over urban and suburban areas.

56 105 *2.1.3 Local binary patterns*

57
58 106 The local binary patterns (LBP) descriptor was proposed by Ojala et al. (1996) to characterize the local
59
60 107 textural features of an image, and has been widely used in the fields of image registration, target

1
2
3
4 108 tracking, etc. The basic idea is to compare the gray value of the center pixel with its neighboring pixels,
5
6 109 so that a set of binary codes of the center pixel can be obtained. Furthermore, improved versions of
7
8 110 LBP were developed with illumination and rotation invariant properties (Ojala et al., 2002). LBP has
9
10 111 been widely applied to characterize the complex urban textures in HR images. For example, Song et al.
11
12 112 (2010) combined the LBP and spectral features to classify HR imagery, and achieved higher accuracy
13
14 113 with the addition of LBP. Musci et al. (2013) extracted the LBP texture features of urban areas from
15
16 114 QuickBird and IKONOS images for land cover classification, and obtained better results compared to
17
18 115 the GLCM features. Li et al. (2015a) extracted local features of HR hyperspectral imagery based on
19
20 116 LBP and obtained good classification results.

21
22 117

23 118 **2.2 Spatial features for high-resolution imagery**

24 25 119 *2.2.1 Pixel shape index*

26
27 120 The pixel shape index (PSI) is a spatial index describing local shape features (Zhang et al., 2006). The
28
29 121 idea of the algorithm is to define a set of anisotropic direction lines radiating from the central pixel to
30
31 122 its surrounding pixels. Under the constraints of the spectrum and the space, the number of neighboring
32
33 123 pixels with spectral similarity to the central pixel along each direction line is counted as the length of
34
35 124 this direction line. The length values of all the directional lines then constitute a histogram, and the
36
37 125 mean value of the histogram is finally defined as the PSI value of the center pixel. PSI can detect more
38
39 126 than 20 directions, which makes up for the insufficient scanning directions of the GLCM and
40
41 127 sufficiently explores the spatial context features in HR images. The authors combined the spectral
42
43 128 information and PSI to conduct urban classification, and demonstrated the superiority of PSI by
44
45 129 comparing it with texture features such as the GLCM and WT. Furthermore, the structural feature set
46
47 130 (SFS) was defined as an extension of PSI based on the histograms of the direction lines, including six
48
49 131 operators such as length-width ratio, weighted PSI, and variance (Huang et al., 2007b). PSI is more
50
51 132 efficient for urban structures than natural surfaces (Huang and Zhang, 2012b), so it is often used as a
52
53 133 local spatial feature together with other features to classify complex urban areas (Li et al., 2017a;
54
55 134 Zhang et al., 2013).

56 135 *2.2.2 PanTex*

57
58 136 PanTex (Pesaresi et al., 2008) is a rotation-invariant built-up presence index computed based on the
59
60 137 GLCM. Specifically, PanTex extracts the GLCM from panchromatic imagery by using the offset

1
2
3
4 138 vectors in 10 directions and the CON measure. Only when the texture values in all the directions are
5
6 139 high can the pixel be considered as a built-up pixel. Therefore, the minimum value of all the directions
7
8 140 is taken as the PanTex value of the pixel. Since PanTex has false alarms from scattered trees,
9
10 141 high-brightness bare soil, rocks, etc., it was further improved by utilizing the normalized difference
11
12 142 vegetation index (NDVI) and morphological filtering, which increased the accuracy by 2.44% and
13
14 143 20.76%, respectively (Pesaresi and Gerhardinger, 2011). This index has also been employed by the
15
16 144 European Commission's Joint Research Centre in the Global Human Settlement Layer (GHSL) project
17
18 145 to extract large-scale built-up areas in Europe from HR images (Florczyk et al., 2016; Pesaresi et al.,
19
20 146 2011; Pesaresi et al., 2013).

21 147 2.2.3 Morphological features

22
23 148 Morphological feature refers to the spatial structure features of an image obtained through basic
24
25 149 morphological operations (e.g., erosion and dilation, opening and closing) with the structural element
26
27 150 (SE). Pesaresi and Benediktsson (2001) proposed the multi-scale morphological profiles (MPs) and
28
29 151 applied it to HR image classification successfully. Since the strength of the morphological feature
30
31 152 response is determined by the SE radius and the local structure size, MPs extracts multi-scale bright
32
33 153 and dark structures of the image with a set of SEs of different sizes (Pesaresi and Benediktsson, 2001).
34
35 154 To detect the morphological features of different scales more effectively, the derivative morphological
36
37 155 profiles (DMPs) were further defined as the sequential differences of the MPs between two adjacent
38
39 156 scales. MPs and DMPs have been utilized for HR image processing in many studies, achieving
40
41 157 satisfactory results (Benediktsson et al., 2003; Chanussot et al., 2006; Chini et al., 2009; Tuia et al.,
42
43 158 2009). In order to apply MPs to hyperspectral imagery, Benediktsson et al. (2005) proposed extended
44
45 159 MPs (EMPs) by using the principal components as the base images to calculate the MPs. Since the
46
47 160 spectral information of hyperspectral imagery was not sufficiently explored by EMPs, Fauvel et al.
48
49 161 (2008) further fused the spectral information and MPs for urban classification. Dalla Mura et al.
50
51 162 (2010b) proposed morphological attribute profiles (APs) to obtain the morphological attributes, such as
52
53 163 area and standard deviation. Similarly, extended APs (EAPs) have also been proposed and applied to
54
55 164 hyperspectral imagery (Dalla Mura et al., 2010a). Huang et al. (2014a) investigated the influence of the
56
57 165 different base image strategies for MPs, and constructed the multiple morphological profiles (MMPs)
58
59 166 for hyperspectral image classification. Ghamisi et al. (2015) reviewed and summarized the different
60
167 morphological features. Since DMPs only consider the difference between adjacent scales and ignore

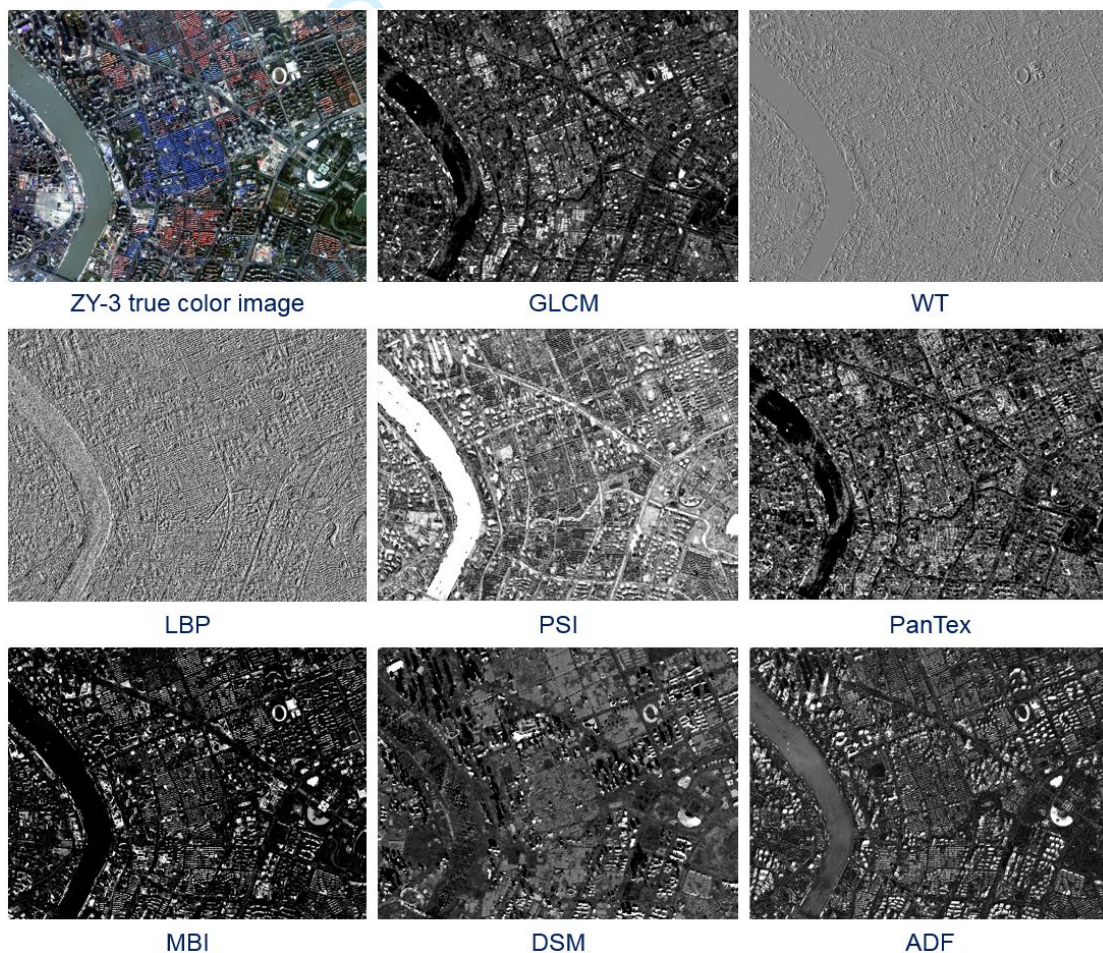
1
2
3
4 168 the cross-scale information, Huang et al. (2016) developed generalized DMPs (GDMPs) to obtain the
5
6 169 difference between arbitrary scales, which can better describe the multi-scale property of complex
7
8 170 urban scenes.

9
10 171 In recent years, the morphological building index (MBI) was proposed for unsupervised building
11
12 172 extraction (Huang and Zhang, 2011). MBI describes the spectral and spatial features of buildings, such
13
14 173 as brightness, structure, and anisotropy, based on morphological operators. Since buildings and their
15
16 174 shadows have similar structures and are spatially adjacent, Huang and Zhang (2012a) also constructed
17
18 175 the morphological shadow index (MSI) for the automatic detection of building shadows. Experiments
19
20 176 were conducted on GeoEye-1, IKONOS, and WorldView-2 images of Wuhan, Hangzhou, and
21
22 177 Washington DC, which confirmed the superiority of this algorithm. The MBI can effectively detect
23
24 178 buildings from HR remote sensing images, but it may also induce false alarms from bright bare ground
25
26 179 and roads. In order to further strengthen the efficacy of the MBI in suburban, mountainous, and
27
28 180 agricultural areas, Huang et al. (2017b) proposed a post-processing framework and obtained more
29
30 181 accurate building extraction results by applying spectral, shadow, and shape constraints successively on
31
32 182 the initial MBI results, to filter out commission errors such as bright vegetation, soil, playgrounds, and
33
34 183 roads. In addition, a number of studies combined the MBI, MSI, and spectral features for urban
35
36 184 classification, built-up area extraction, change detection, etc. (Huang et al., 2017a; Li et al., 2017a;
37
38 185 Wen et al., 2016; Zhang and Huang, 2018; Liu et al., 2019), confirming the effectiveness of these
39
40 186 indices in urban feature extraction.

41 187 *2.2.4 Stereo features*

42
43 188 HR stereo observation satellites can acquire images from multiple viewing angles, which can be
44
45 189 employed to produce a digital surface model (DSM), and applied to height estimation and 3D
46
47 190 reconstruction. In recent years, many researchers have found that the application of stereo features, e.g.,
48
49 191 a DSM, to urban classification can increase the separability of land cover types such as building
50
51 192 structures and roads (Longbotham et al., 2012; Peng et al., 2015; Qin, 2014; Qin and Fang, 2014; Tian
52
53 193 et al., 2014). In terms of the fact that the elevation of roads, grassland, and bare land are relatively
54
55 194 consistent while buildings have abrupt changes to the surrounding ground surface, Peng et al. (2017)
56
57 195 proposed the stereo pair disparity index (SPDI) to extract built-up areas by describing the intensity of
58
59 196 the elevation change. This method firstly generates disparity maps from multi-view images by using
60
197 stereo matching algorithm (e.g., semiglobal matching), and then calculates the disparity gradients with

198 multi-directional offset vectors. Finally, the built-up areas can be extracted from the gradient features.
 199 However, in dense urban areas, the quality of a DSM or disparity map is susceptible to many factors
 200 such as the base-height ratio, the image matching algorithm, and occlusions, which further influence
 201 the accuracy of urban information extraction. In order to fully exploit the angular information of HR
 202 stereo imagery, Huang et al. (2018b) proposed the angular difference feature (ADF) to describe the
 203 dissimilarities between different viewing images from the pixel, feature, and label levels. The ZY-3
 204 multi-angle images were utilized in the experiments, and the results indicated that the joint use of ADF
 205 and spectral features can significantly improve urban classification accuracy, and the ADF can help to
 206 distinguish complex artificial structures with spectral similarity (e.g., roads, high-rise houses, urban
 207 villages, and residential buildings).



208
 209 Figure 2 Illustrations of the typical spatial features extracted from ZY-3 stereo imagery in central
 210 Shanghai.

211 Demonstrations of some typical spatial features are displayed in Figure 2. The eight textural,
 212 structural and stereo features were extracted from ZY-3 imagery in central Shanghai. Note that the
 213 stereo features (DSM and ADF) were generated from multi-view images, while the remaining features

214 were calculated from the nadir panchromatic image.

215

216 **2.3 Deep learning-based feature representation**

217 The previous features were designed based mainly on domain-specific knowledge. Nevertheless, their
218 discriminative ability may still be limited to tackle complex or large-scale urban analysis. In recent
219 years, deep learning-based methods have been increasingly investigated in the field of remote sensing,
220 such as land use classification (Huang et al., 2018a), scene recognition (Li et al., 2017c), and urban
221 expansion monitoring (He et al., 2019). Unlike handcrafted features, deep neural networks (DNNs) can
222 directly extract high-level features from data based on neural networks with deep architecture in an
223 automated fashion (Reichstein, et al., 2019; Zhu, et al., 2017). Sufficient learning of a deep neural
224 network is very difficult and costly since it relies on massive samples and computational resources. The
225 pre-training and fine-tuning strategies are widely adopted (Li et al., 2019). For instance, Marmanis et
226 al. (2016) directly extracted the features by transferring the convolutional neural networks (CNNs)
227 pre-trained on natural images (e.g., ImageNet) for HR remote sensing scene classification. Hu et al.
228 (2015) proposed two scenarios to generate global feature representations for HR image scenes by using
229 the CNNs, which achieved remarkable classification accuracies on two public HR datasets. Nogueira et
230 al. (2017) adapted the existing CNN architectures to HR image classification by fine-tuning with a
231 small sample set of HR images, demonstrating the effectiveness of fine-tuned networks for
232 performance improvements compared with using only the pre-trained networks.

233

234 **3. Urban information extraction from high-resolution remote sensing imagery**

235 **3.1 Target recognition**

236 Target recognition is one of the major tasks of information extraction. Urban targets, mainly including
237 buildings, built-up, impervious surface, roads, vegetation, and water bodies, are of great interest to
238 researchers and city planners since they are vital indicators of human distribution, economic
239 development and city's livability (Weng, 2012). With the availability of HR data, these detailed targets
240 are now possible to be recognized. Numerous approaches have been proposed to extract the thematic
241 information of the urban target of interest. In this section, some representative methods are briefly
242 introduced.

243 *3.1.1 Impervious surfaces, buildings, and roads*

1
2
3
4 244 Impervious surface, or other similar semantic abstractions such as artificial surfaces, urban footprint,
5
6 245 human settlement, and built-up areas, are the major components of urban land. A large amount of
7
8 246 researches have been focused on impervious surface extraction from coarse and medium resolution
9
10 247 images over large areas (Chen et al., 2016; Li et al., 2015b; Schneider et al., 2010; Weng, 2012). HR
11
12 248 imagery can significantly reduce the problems of mixed-pixels and blurred boundaries but also brings
13
14 249 new challenges, such as the confusion between different ground objects (e.g., bright impervious layers
15
16 250 and bare soil, dark impervious layers and water) and the problems brought by shadows. To address
17
18 251 these issues, Hu and Weng (2011) proposed an object-based method to extract impervious surfaces for
19
20 252 residential and central business district (CBD) areas from IKONOS imagery, which obtained high
21
22 253 accuracies and precise feature boundaries. The attributes considered in the rule set included spectral,
23
24 254 spatial, and textural features, which were used to comprehensively describe the properties of
25
26 255 impervious surfaces. To tackle the underestimation of impervious area caused by shadows, Zhang and
27
28 256 Huang (2018) presented a two-stage object-based framework by integrating multiple features.
29
30 257 Specifically, the spatial relationships of different land covers (e.g., the distance between shadow and
31
32 258 vegetation) were further considered in the second stage to extract more detailed impervious surface
33
34 259 information in shaded areas. Since synthetic aperture radar (SAR) is sensitive to the structural or
35
36 260 geometric features of built environment, integration of optical and SAR images at pixel, feature, and
37
38 261 decision levels are explored to improve the estimation of impervious layers (Shao et al., 2016; Zhang et
39
40 262 al., 2014). More recently, Liu et al. (2019) proposed a framework for built-up extraction by
41
42 263 characterizing building properties from structural, textural and vertical aspects, demonstrating the
43
44 264 complementation of multi-feature fusion. It was also suggested that the employ of stereo features can
45
46 265 effectively reduce the omission errors of dark built-up areas.

46 266 For building extraction, knowledge-based automatic approaches, which construct the building
47
48 267 extraction rules by considering the spectral, shape, texture, and spatial characteristics of buildings, are
49
50 268 commonly adopted. Generally, the sizes of most urban buildings are within a certain range; buildings
51
52 269 have vertical structures and high reflectivity; buildings and their shadows are spatially adjacent (Huang
53
54 270 et al., 2017b; Pesaresi et al., 2008). These characteristics have been extensively exploited to infer the
55
56 271 existence of buildings in HR images, by characterizing the brightness, local contrast, shape, height, and
57
58 272 the spatial relationships between buildings and their shadows with the information of solar incident
59
60 273 angle. For instance, in Ok et al. (2013), the shadow areas in the image were firstly extracted, then the

1
2
3
4 274 candidate buildings were detected according to the spatial directional relationship of shadows and
5
6 275 buildings. Since this method highly dependent on initial shadow extraction accuracy, post-processing
7
8 276 and optimization of the shadow were conducted in Ok (2013) in order to further improve building
9
10 277 detection accuracy. The MBI and MSI discussed in Section 2.2.3 were also employed in many studies
11
12 278 for automatic building detection (Huang and Zhang, 2012a). When dealing with complex urban scenes,
13
14 279 supervised approaches are widely used for building extraction. For example, the widely used
15
16 280 object-oriented multi-feature fusion methods, for which the selection of the segmentation scale and
17
18 281 feature extraction are the two important steps. The optimization of the segmentation scale ensures the
19
20 282 independence and integrity of the extracted buildings (Tian and Chen, 2007), while spectral, texture,
21
22 283 shape and stereo features are commonly applied to depict the within-object information (Fauvel et al.,
23
24 284 2008; Liu et al., 2017; Zhang et al., 2017).

25 285 Road detection from HR images is a challenging task because of the spectral and spatial
26
27 286 complexity of road networks. Similar to building extraction, the spectrum, shape, and topology
28
29 287 properties of road are extensively considered. For example, roads generally present a curvilinear shape;
30
31 288 the width of a road does not change drastically; and roads have apparent edge lines and crossings, and
32
33 289 often form networks. Based on this knowledge, Huang and Zhang (2009) proposed an object-based
34
35 290 method to extract road centerlines from HR imagery, by integrating multi-scale spectral-structural
36
37 291 information based on support vector machine (SVM). Poullis (2014) presented an automatic road
38
39 292 extraction method that combined tensor encoding, Gabor filter, and Graph-Cuts for the inference of
40
41 293 road features. Shanmugam and Kaliaperumal (2015) proposed the active deformable model for
42
43 294 semi-automatic road extraction. This method first selected the road seed points manually, from which
44
45 295 the propagation started and was restrained by the width and color of the road. Then, the interconnected
46
47 296 road networks can be extracted. Sghaier and Lepage (2016) applied the beamlet transform in road
48
49 297 border detection to find the most suitable scale for each road in HR image. The SFS structural feature,
50
51 298 mathematical morphology, and Canny detector were also employed in preprocessing steps for edge
52
53 299 candidate selection.

54 300 3.1.2 *Urban vegetation and water areas*

55
56 301 Vegetation and water have distinct spectral characteristics, hence some classic spectral indices, such as
57
58 302 the normalized difference vegetation index (NDVI), the normalized difference water index (NDWI),
59
60 303 and the modified NDWI (MNDWI), were designed for their detection based on simple band operations.

1
2
3
4 304 However, most of the existing indices are not very appropriate to be directly applied to HR images in
5
6 305 urban environment due to the spectral similarity of some urban structures (e.g., temporary building,
7
8 306 shadow) which also show high response of these indices. Moreover, many HR imagery have only four
9
10 307 spectral bands (i.e., blue, green, red, near-infrared), hence lack the prerequisite channel to calculate
11
12 308 some indices (e.g., MNDWI). To tackle these problems, Kumar et al. (2012) created a new vegetation
13
14 309 index by taking advantages of the NIR-2 and red edge bands of WorldView-2 imagery to extract
15
16 310 vegetation, which obtained improved accuracy compared to the conventional NDVI. Xie et al. (2016)
17
18 311 proposed a HR water index based on combinations of WorldView-2 eight-band data. This new water
19
20 312 index was further combined with the MSI, in order to alleviate the disturbance from shadows.
21
22 313 According to their tests, the water index calculated by coastal-NIR2 or green-NIR2 bands achieved the
23
24 314 best performance to highlight urban water areas in multiple big cities.

25
26 315 In addition to the binary extraction of vegetation and water, some studies further concerned the
27
28 316 identification of their subclasses. For instance, Wen et al. (2017) conducted semantic classification of
29
30 317 the urban tree functions from HR imagery. Unlike general vegetation extraction and tree species
31
32 318 classification, this study considered the location and function of trees, by dividing trees into park trees,
33
34 319 roadside trees and residential-institutional trees based on a multi-level framework (pixel-object-patch).
35
36 320 Specifically, the vegetation index was firstly calculated for vegetation extraction at the pixel level.
37
38 321 Object-oriented segmentation was then performed over the vegetated area, and the spectral and texture
39
40 322 features were extracted at the object level to distinguish between trees and ground vegetation. Finally,
41
42 323 the semantic functions of the trees were obtained based on the area, shape, structure, and spatial
43
44 324 relationships at the patch level. Huang et al. (2015b) identified different water-body types including
45
46 325 lakes, rivers, canals and ponds in Wuhan and Shenzhen. A two-layer machine learning framework was
47
48 326 presented, which first detected preliminary water areas by using water, shadow, and vegetation indices.
49
50 327 The geometrical and textural features were then extracted at the object level, and the different urban
51
52 328 water types were finally identified.

53
54 329 In general, courtesy of the rich spatial details in HR imagery, massive efforts have been devoted to
55
56 330 propose automatic or semi-automatic approaches for urban object extraction, by characterizing the
57
58 331 physical properties (i.e., texture, shape, height) of the target of interest. Although impressive results
59
60 332 were obtained, their applicability may be limited since the spatial contexts of complex and varying
333 urban scenes are often difficult to be described as a set of “rules”. Current studies that integrate domain

334 knowledge with machine learning techniques (e.g., deep learning) show a promising direction for urban
335 target detection from HR imagery (Zhou et al., 2016; Zhu et al., 2017).

336

337 **3.2 Land use/land cover mapping**

338 Urban land use/land cover (LULC) information are crucial data to understand the complex interactions
339 between human and the environment (Kuang et al., 2016; Yu et al., 2016). Land cover focuses on the
340 physical property of the land surface, e.g., impervious surfaces, vegetation and water, while land use
341 places emphasis on the social functional attributes, such as residential, industrial or commercial.
342 Numerous methods have been proposed for LULC mapping, which can generally be categorized into
343 three types according to their basic processing units (i.e. pixels, objects, and moving windows). Pixel-
344 and object-based approaches are widely used for land cover mapping (Myint et al., 2011). While
345 classifying land use is more difficult since it relates to human activities and one land use type is often
346 mixed by multiple land covers. The texture, geometry, contexture, land cover proportion, or other
347 auxiliary data (e.g., Google Street View) are often incorporated to recognize land use patterns and
348 configurations (Li et al., 2017b; Zhang et al., 2019). Machine learning techniques for supervised
349 classification have been extensively exploited for urban LULC mapping from HR imagery, such as the
350 classification and regression tree (CART), *k*-nearest neighbor (KNN), random forest (RF), SVM, and
351 multilayer perceptron (MLP) (Qian et al., 2015; Zhang and Huang, 2018). Since traditional low-level
352 features may be insufficient to characterize urban land use, mid-level features are constructed by means
353 of dictionary learning and sparse coding such as the popular bag-of-visual-words (BOVW) and latent
354 Dirichlet allocation (LDA) models. Based on these scene models, Huang et al. (2015a) extracted the
355 urban villages from QuickBird and WorldView-2 images covering Wuhan and Shenzhen; Zhang and
356 Du (2015) employed city blocks as the processing unit to map the urban functional zones in Zhuhai and
357 Beijing. Moreover, a variety of landscape metrics were calculated in order to better describe complex
358 urban scenes. For example, Voltersen et al. (2014) combined HR images and a normalized DSM
359 (nDSM) to classify basic urban features. Several landscape metrics of buildings and vegetation, e.g.,
360 volume, height, and vegetation fraction, were then extracted at the block level to describe the urban
361 structure types, dividing the urban land use into residential, commercial, and industrial areas, parks,
362 woodland, etc. Liu et al. (2017) correlated the physical structure properties of urban villages (e.g., high
363 building density and scarce vegetation) and the landscape metrics for urban village mapping. Recently,

364 more endeavors have been devoted to employ the new deep learning methods for LULC mapping,
365 which achieved state-of-the-art performances by learning the most discriminative features
366 hierarchically (Huang et al., 2018a; Zhang et al., 2019; Zhu, et al., 2017).

368 3.3 Change detection

369 In developing regions, many cities are undergoing rapid urban expansion as well as internal formation
370 and demolition. Timely and efficient monitoring of urban changes helps us to understand human
371 activity and provide a decision-making basis for urban planning (Marin et al., 2015). HR remote
372 sensing imagery enables detection of subtle urban changes, but also poses great difficulties to the
373 traditional methods. The major challenge of change detection from HR imagery is the confusion of
374 radiometric and real semantic changes. False alarms are mainly induced by the distinct spectral
375 heterogeneity of the multi-temporal HR images (i.e., the spectral behavior of the same object varies at
376 different dates), due to different imaging conditions, mis-registration, disparity of vertical structures,
377 etc. (Bruzzone and Bovolo, 2012). The widely used change detection methods include machine
378 learning approaches (Volpi et al., 2013) and automatic methods such as the multilevel change vector
379 analysis (Bovolo, 2009), the pulse-coupled neural networks (Pacifici and Del Frate, 2010), and the
380 multi-temporal morphological attribute profiles (Falco et al., 2013). In order to tackle the problems of
381 spectral complexity and mis-registration of the multi-temporal HR images, Wen et al. (2016) employed
382 several basic urban primitives (building, vegetation, and water) to represent complex urban scenes and
383 utilized blocks as the basic unit to calculate their composition and arrangement. The information of the
384 primitive features in the corresponding blocks between multi-temporal images were compared, then the
385 changed area and type can be identified. In addition, Huang et al. (2017a) proposed a multi-level (pixel,
386 grid, and city block) framework for urban change analysis from HR images. The ZY-3 stereo images
387 were employed to produce the multi-temporal orthographic images covering Wuhan and Beijing, and
388 the multi-features and rules were integrated for land cover classification. The authors also compared
389 the results of ZY-3 and Landsat images, suggesting that HR imagery was indispensable for subtle urban
390 change detection.

392 3.4 Ecology and climate analysis

393 Urban LULC types have profound impacts on the urban ecological environment and climate (Kuang et

1
2
3
4 394 al., 2017; Shi et al., 2016). On the basis of LULC data, more in-depth information of a city can be
5
6 395 explored, such as the quantitative assessment of ecosystem service capacities or simulation of local
7
8 396 climate. Burkhard et al. (2012) proposed a clear and applicable conceptual framework for ecosystem
9
10 397 service mapping. The authors linked the different land cover types to ecosystem service supply and
11
12 398 demand, and synthesized the expert knowledge from many studies to give the capacity scores of
13
14 399 different land cover types. Following the ecosystem service concept and assessment scheme, Haas and
15
16 400 Ban (2017) assessed the ecological changes in the urban core districts of Shanghai in China. The
17
18 401 authors first generated the basic urban LULC types from multi-temporal IKONOS and GeoEye-1
19
20 402 images. The LULC changes were then analyzed in terms of ecosystem service supply and demand, and
21
22 403 the ecosystem balance of central Shanghai from 2000 to 2009 was modeled.

23 404 On the other hand, the distribution and variation of the urban climate have received broad
24
25 405 attention, as the urban climate is closely related to environmental and human health issues. The dense
26
27 406 population and heterogeneous landscapes in urban areas make the intra-urban climate distinctly
28
29 407 different. Stewart and Oke (2012) introduced a universal classification scheme for the land surface,
30
31 408 called local climate zones (LCZ), for urban climate studies. According to the building properties (e.g.,
32
33 409 height, density, material), the LCZ system classifies 10 built types, such as compact high-rise, open
34
35 410 low-rise, and heavy industry. Meanwhile, seven land cover categories, including dense trees, low
36
37 411 plants, water, etc., are also defined to represent natural landscapes. The spatial scale of LCZ studies is
38
39 412 generally between 100 and 1000 m. Bechtel et al. (2015) investigated the feasibility of using remote
40
41 413 sensing imagery for LCZ mapping, and developed the World Urban Database and Access Portal Tools
42
43 414 (WUDAPT) for global HR LCZ mapping. Some follow-up studies were carried out, for instance,
44
45 415 Bechtel et al. (2016) integrated multispectral data and SAR imagery for LCZ mapping in arid areas.
46
47 416 Wang et al. (2018) performed LCZ classification in arid desert cities using open-source image data and
48
49 417 software. The LCZ properties were evaluated and compared to the original value ranges in Stewart and
50
51 418 Oke (2012), and their relationships with the surface urban heat island effect were also analyzed.

52 419

53 54 420 **4. Conclusions and perspectives**

55
56
57 421 As an emerging research field, the development of high-resolution (HR) urban remote sensing is
58
59 422 inseparable from sensor technology, photogrammetry, image processing technique, etc.

1
2
3
4 423 High-resolution, multi-temporal, multi-angle, and multi-platform urban observations allow more
5
6 424 elaborate urban application, which also call for more effective data interpretation approaches. In this
7
8 425 paper, we examined the major advances in HR urban remote sensing from the feature level to the scene
9
10 426 level. A series of advanced textural, structural and stereo features, as well as the new techniques for
11
12 427 urban information extraction were summarized. Although HR urban remote sensing has achieved
13
14 428 substantial improvements, many of the existing researches only involve small-scale applications and
15
16 429 their robustness and generalization ability are unproved. There are still great challenges to meet the
17
18 430 requirements of practical production or commercialization. The trends for future development are
19
20 431 discussed from the following perspectives:

21 432 1) *Progress in methodology*: Recent developments in machine learning, especially deep learning,
22
23 433 have achieved notable success in plenty of scientific fields. For instance, convolutional neural
24
25 434 networks (CNNs) and recurrent neural networks (RNNs) are the two important branches for spatial
26
27 435 learning and sequence learning, respectively, which are highly effective in urban remote sensing
28
29 436 tasks. Nevertheless, applying deep learning to remotely sensed image interpretation is still in its
30
31 437 infancy mainly due to the strong data heterogeneity, inadequate sample annotation, and high
32
33 438 complexity of the model. Specialized training datasets for HR remote sensing imagery are still few
34
35 439 in number. There is an urgent need for creating large-volume benchmark data with abundant,
36
37 440 diverse, and reliable representation of various urban landscapes. Unsupervised, semi-supervised, or
38
39 441 weakly supervised learning approaches are also promising to reduce the work of manual
40
41 442 annotation.

42 443 2) *Characterizing urban structure and pattern*: Identifying the internal pattern, configuration or
43
44 444 functional attributes (e.g., commercial/residential/industrial areas, urban villages,
45
46 445 ecological/leisure land) of urban land is significant for effective urban management and planning.
47
48 446 By virtue of HR stereo imagery (e.g., ZY-3, WorldView), 3D urban form can be conveniently
49
50 447 derived, which can support the future researches on urban dynamics in both horizontal and vertical
51
52 448 dimensions, as well as providing new avenues for multidisciplinary applications such as
53
54 449 socioeconomic research, disaster response, environmental assessment, and ecological modelling.

55
56 450 3) *Big data challenge*: The astonishing geospatial data acquisition ability and the trend of elaborating
57
58 451 urban information extraction over time and space calls for increased computational power to
59
60 452 address the big data challenges (Ma et al., 2015). The abundant high-performance computing

resources and cloud technology offer promising solutions (Li et al., 2016; Sun et al., 2019). One such example is GEE (Gorelick et al., 2017), which has archived petabytes of EO data and allows interactive data process and algorithm development over its online system, facilitating lots of researchers to carry out global or continental urban mapping and studies (Gong et al., 2019a; Gong et al., 2019b; Liu et al., 2018).

4) *Global mapping*: The exponentially growing HR data facilitates urban remote sensing towards larger scales hence increase our knowledge about the fast urbanizing world. Historically, urban mapping at the global scale are mostly relied on coarse resolution imagery (e.g., MODIS). With the availability of the global Landsat archives, some fine resolution global products were generated in recent years, such as the FROM-GLC30 (Gong et al., 2013), GlobeLand30 (Chen et al., 2015), GHSL (Pesaresi et al., 2015), and MGIS (Liu et al., 2018), which provide us valuable information about the location and extent of urban areas worldwide. More recently, the global land cover map at 10 m resolution, i.e., FROM-GLC10 (Gong et al., 2019), was derived from Sentinel-2 data at so far the highest spatial resolution. In addition, new satellites, such as GaoFen series, ZY-3 constellation, PlanetScope, and Luojia-1, can acquire optical, SAR and nighttime light data at high spatial/temporal resolution, which have great potentials for global urban information extraction in the future.

Acknowledgements This work was supported by the National Natural Science Foundation of China (Grant Nos. 41771360 & 41842035), the National Program for Support of Top-notch Young Professionals, the Hubei Provincial Natural Science Foundation of China (Grant No. 2017CFA029), the National Key Research and Development Program of China (Grant No. 2016YFB0501403), and the Shenzhen Science and Technology Program (Grant No. JCYJ20180306170645080).

References

- Bechtel B, Alexander P J, Boehner J, Ching J, Conrad O, Feddema J, Mills G, See L, Stewart I. 2015. Mapping local climate zones for a worldwide database of the form and function of cities. *ISPRS Int Geo-Inf*, 4: 199-219
- Bechtel B, See L, Mills G, Foley M. 2016. Classification of local climate zones using SAR and multispectral data in an arid environment. *IEEE J Sel Top Appl Earth Observ Remote Sens*, 9: 3097-3105
- Benediktsson J A, Palmason J A, Sveinsson J R. 2005. Classification of hyperspectral data from urban areas based on extended morphological profiles. *IEEE Trans Geosci Remote Sensing*, 43: 480-491
- Benediktsson J A, Pesaresi M, Amason K. 2003. Classification and feature extraction for remote

- 1
2
3 487 sensing images from urban areas based on morphological transformations. *IEEE Trans Geosci*
4 488 *Remote Sensing*, 41: 1940-1949
- 5
6 489 Bovolo F. 2009. A multilevel parcel-based approach to change detection in very high resolution
7 490 multitemporal images. *IEEE Geosci Remote Sens Lett*, 6: 33–37
- 8
9 491 Bruzzone L, Bovolo F. 2012. A novel framework for the design of change-detection systems for
10 492 very-high-resolution remote sensing images. *Proceedings of the IEEE*. 101: 609-630
- 11
12 493 Burkhard B, Kroll F, Nedkov S, Mueller F. 2012. Mapping ecosystem service supply, demand and
13 494 budgets. *Ecol Indic*, 21: 17-29
- 14
15 495 Chanussot J, Benediktsson J A, Fauvel M. 2006. Classification of remote sensing images from urban
16 496 areas using a fuzzy possibilistic model. *IEEE Geosci Remote Sens Lett*, 3: 40-44
- 17
18 497 Chen J, Chen J, Liao A Pa, Cao X, Chen L J, Chen X H, He C Y, Han G, Peng S, Lu M, Zhang W W,
19 498 Tong X H, Mills J. 2015. Global land cover mapping at 30m resolution: A POK-based operational
20 499 approach. *ISPRS J Photogramm Remote Sens*, 103:7-27
- 21
22 500 Chen X H, Cao X, Liao A P, Chen L J, Peng S, Lu M, Chen J, Zhang W W, Zhang H W, Han G, Wu
23 501 H, Li R. 2016. Global mapping of artificial surfaces at 30-m resolution. *Sci China Earth Sci*:
24 502 59:2295-2306
- 25
26 503 Chini M, Pierdicca N, Emery W J. 2009. Exploiting SAR and VHR optical images to quantify damage
27 504 caused by the 2003 Bam earthquake. *IEEE Trans Geosci Remote Sensing*, 47: 145-152
- 28
29 505 Dalla Mura M, Benediktsson J A, Waske B, Bruzzone L. 2010a. Extended profiles with morphological
30 506 attribute filters for the analysis of hyperspectral data. *Int J Remote Sens*, 31: 5975-5991
- 31
32 507 Dalla Mura M, Benediktsson J A, Waske B, Bruzzone L. 2010b. Morphological attribute profiles for
33 508 the analysis of very high resolution images. *IEEE Trans Geosci Remote Sensing*, 48: 3747-3762
- 34
35 509 Falco N, Mura M D, Bovolo F, Benediktsson J A, Bruzzone L. 2013. Change detection in VHR images
36 510 based on morphological attribute profiles. *IEEE Geosci Remote Sens Lett*, 10: 636–640
- 37
38 511 Fauvel M, Benediktsson J A, Chanussot J, Sveinsson J R. 2008. Spectral and spatial classification of
39 512 hyperspectral data using SVMs and morphological profiles. *IEEE Trans Geosci Remote Sensing*,
40 513 46: 3804-3814
- 41
42 514 Florczyk A J, Ferri S, Syrris V, Kemper T, Halkia M, Soille P, Pesaresi M. 2016. A new European
43 515 settlement map from optical remotely sensed data. *IEEE J Sel Top Appl Earth Observ Remote Sens*,
44 516 9: 1978-1992
- 45
46 517 Gamba P, Herold M. 2009. *Global mapping of human settlement: experiences, datasets, and prospects*.
47 518 CRC Press. 374
- 48
49 519 Ghamisi P, Dalla Mura M, Benediktsson J A. 2015. A survey on spectral–spatial classification
50 520 techniques based on attribute profiles. *IEEE Trans Geosci Remote Sensing*, 53: 2335-2353
- 51
52 521 Gong P, Li X C, Zhang W. 2019a. 40-Year (1978–2017) human settlement changes in China reflected
53 522 by impervious surfaces from satellite remote sensing. *Sci Bull*, 64: 756–763
- 54
55 523 Gong P, Liang S, Carlton E J, Jiang Q, Wu J, Wang L, Remais J V. 2012. Urbanisation and health in
56 524 China. *Lancet*, 379: 843-852
- 57
58 525 Gong P, Liu H, Zhang M, Li C, Wang J, Huang H, Clinton N, Ji L, Li W, Bai Y, Chen B, Xu B, Zhu Z,
59 526 Yuan C, Suen H P, Guo J, Xu N, Li W, Zhao Y, Yang J, Yu C, Wang X, Fu H, Yu L, Dronova I,
60 527 Hui F, Cheng X, Shi X, Xiao F, Liu Q, Song L. 2019b. Stable classification with limited sample:
528 transferring a 30-m resolution sample set collected in 2015 to mapping 10-m resolution global land
529 cover in 2017. *Sci Bull*, 64: 370–373
- 530
531 530 Gong P, Wang J, Yu L, Zhao Y, Zhao Y, Liang L, Niu Z, Huang X, Fu H, Liu S, Li C, Li X, Fu W, Liu

- 1
2
3 531 C, Xu Y, Wang X, Cheng Q, Hu L, Yao W, Zhang H, Zhu P, Zhao Z, Zhang H, Zheng Y, Ji L,
4 532 Zhang Y, Chen H, Yan A, Guo J, Yu L, Wang L, Liu X, Shi T, Zhu M, Chen Y, Yang G, Tang P,
5 533 Xu B, Giri C, Clinton N, Zhu Z, Chen J, Chen J. 2013. Finer resolution observation and monitoring
6 534 of global land cover: first mapping results with Landsat TM and ETM+ data. *Int J Remote Sens*, 34:
7 535 2607-2654
- 8
9
10 536 Gorelick N, Hancher M, Dixon M, Ilyushchenko S, Thau D, Moore R. 2017. Google Earth Engine:
11 537 Planetary-scale geospatial analysis for everyone. *Remote Sens Environ*, 202: 18-27
- 12 538 Guo X, Huang X, Zhang L. 2014. Three-dimensional wavelet texture feature extraction and
13 539 classification for multi/hyperspectral imagery. *IEEE Geosci Remote Sens Lett*, 11: 2183-2187
- 14 540 Haas J, Ban Y. 2017. Mapping and monitoring urban ecosystem services using multitemporal
15 541 high-resolution satellite data. *IEEE J Sel Top Appl Earth Observ Remote Sens*, 10: 669-680
- 16 542 Haralick R M, Shanmugam K. 1973. Textural features for image classification. *IEEE Trans Syst Man*
17 543 *Cybern*, 610-621
- 18 544 He C, Liu Z, Gou S, Zhang Q, Zhang J, Xu L. 2019. Detecting global urban expansion over the last
19 545 three decades using a fully convolutional network. *Environ Res Lett*, 14: 034008
- 20 546 Hu F, Xia G S, Hu J, Zhang L. 2015. Transferring deep convolutional neural networks for the scene
21 547 classification of high-resolution remote sensing imagery. *Remote Sens*, 7:14680-14707
- 22 548 Hu X, Weng Q. 2011. Impervious surface area extraction from IKONOS imagery using an
23 549 object-based fuzzy method. *Geocarto Int*, 26: 3-20
- 24 550 Huang B, Zhao B, Song Y. 2018a. Urban land-use mapping using a deep convolutional neural network
25 551 with high spatial resolution multispectral remote sensing imagery. *Remote Sens Environ*, 214:
26 552 73-86
- 27 553 Huang J K, Zhu L F, Deng X Z. 2007. Regional differences and determinants of built-up area
28 554 expansion in China. *Sci China Earth Sci*, 50: 1835-1843
- 29 555 Huang X, Chen H, Gong J. 2018b. Angular difference feature extraction for urban scene classification
30 556 using ZY-3 multi-angle high-resolution satellite imagery. *ISPRS-J Photogramm Remote Sens*, 135:
31 557 127-141
- 32 558 Huang X, Guan X, Benediktsson J A, Zhang L, Li J, Plaza A, Dalla Mura M. 2014a. Multiple
33 559 morphological profiles from multicomponent-base images for hyperspectral image classification.
34 560 *IEEE J Sel Top Appl Earth Observ Remote Sens*, 7: 4653-4669
- 35 561 Huang X, Han X, Zhang L, Gong J, Liao W, Benediktsson J A. 2016. Generalized differential
36 562 morphological profiles for remote sensing image classification. *IEEE J Sel Top Appl Earth Observ*
37 563 *Remote Sens*, 9: 1736-1751
- 38 564 Huang X, Liu H, Zhang L. 2015a. Spatiotemporal detection and analysis of urban villages in mega city
39 565 regions of China using high-resolution remotely sensed imagery. *IEEE Trans Geosci Remote*
40 566 *Sensing*, 53: 3639-3657
- 41 567 Huang X, Liu X, Zhang L. 2014b. A multichannel gray level co-occurrence matrix for
42 568 multi/hyperspectral image texture representation. *Remote Sens*, 6: 8424-8445
- 43 569 Huang X, Wen D, Li J, Qin R. 2017a. Multi-level monitoring of subtle urban changes for the
44 570 megacities of China using high-resolution multi-view satellite imagery. *Remote Sens Environ*, 196:
45 571 56-75
- 46 572 Huang X, Xie C, Fang X, Zhang L. 2015b. Combining pixel- and object-based machine learning for
47 573 identification of water-body types from urban high-resolution remote-sensing imagery. *IEEE J Sel*
48 574 *Top Appl Earth Observ Remote Sens*, 8: 2097-2110

- 1
2
3 575 Huang X, Yuan W, Li J, Zhang L. 2017b. A new building extraction postprocessing framework for
4 576 high-spatial-resolution remote-sensing imagery. *IEEE J Sel Top Appl Earth Observ Remote Sens*,
5 577 10: 654-668
- 6 578 Huang X, Zhang L. 2009. Road centreline extraction from high-resolution imagery based on multiscale
7 579 structural features and support vector machines. *Int J Remote Sens*, 30: 1977-1987
- 8 580 Huang X, Zhang L. 2011. A multidirectional and multiscale morphological index for automatic
9 581 building extraction from multispectral GeoEye-1 imagery. *Photogramm Eng Remote Sens*, 77:
10 582 721-732
- 11 583 Huang X, Zhang L. 2012a. Morphological building/shadow index for building extraction from
12 584 high-resolution imagery over urban areas. *IEEE J Sel Top Appl Earth Observ Remote Sens*, 5:
13 585 161-172
- 14 586 Huang X, Zhang L. 2012b. A multiscale urban complexity index based on 3D wavelet transform for
15 587 spectral-spatial feature extraction and classification: an evaluation on the 8-channel WorldView-2
16 588 imagery. *Int J Remote Sens*, 33: 2641-2656
- 17 589 Huang X, Zhang L, Li P. 2007a. An adaptive multiscale information fusion approach for feature
18 590 extraction and classification of IKONOS multispectral imagery over urban areas. *IEEE Geosci*
19 591 *Remote Sens Lett*, 4: 654-658
- 20 592 Huang X, Zhang L, Li P. 2007b. Classification and extraction of spatial features in urban areas using
21 593 high-resolution multispectral imagery. *IEEE Geosci Remote Sens Lett*, 4: 260-264
- 22 594 Kuang W H, Chen L J, Liu J Y, Xiang W N, Chi W F, Lu D S, Yang T R, Pan T, Liu A L. 2016.
23 595 Remote sensing-based artificial surface cover classification in Asia and spatial pattern analysis. *Sci*
24 596 *China Earth Sci*, 59: 1720-1737
- 25 597 Kuang W H, Yang T R, Liu A L, Zhang C, Lu D S, Chi W F. 2017. An EcoCity model for regulating
26 598 urban land cover structure and thermal environment: Taking Beijing as an example. *Sci China Earth*
27 599 *Sci*, 60: 1098-1109
- 30 600 Kumar A, Pandey A C, Jeyaseelan A T. 2012. Built-up and vegetation extraction and density mapping
31 601 using WorldView-II. *Geocarto Int*, 27: 557-568
- 32 602 Li J, Huang X, Gong J. 2019. Deep neural network for remote sensing image interpretation: status and
33 603 perspectives. *Natl Sci Rev*, 0: 1-4. doi: 10.1093/nsr/nwz058
- 34 604 Li Q, Huang X, Wen D, Liu H. 2017a. Integrating multiple textural features for remote sensing image
35 605 change detection. *Photogramm Eng Remote Sens*, 83: 109-121
- 36 606 Li S, Dragicevic S, Castro F A, Sester M, Winter S, Coltekin A, Pettit C, Jiang B, Haworth J, Stein A,
37 607 Cheng T. 2016. Geospatial big data handling theory and methods: a review and research challenges.
38 608 *ISPRS-J Photogramm Remote Sens*, 115: 119-133
- 39 609 Li W, Chen C, Su H, Du Q. 2015a. Local binary patterns and extreme learning machine for
40 610 hyperspectral imagery classification. *IEEE Trans Geosci Remote Sensing*, 53: 3681-3693
- 41 611 Li X, Gong P, Liang L. 2015b. A 30-year (1984–2013) record of annual urban dynamics of Beijing
42 612 City derived from Landsat data. *Remote Sens Environ*, 166: 78–90
- 43 613 Li X, Zhang C, Li W. 2017b. Building block level urban land-use information retrieval based on
44 614 Google Street View images. *GISci Remote Sens*, 54: 819-835
- 45 615 Li Y S, Huang X, Liu H. 2017c. Unsupervised deep feature learning for urban village detection from
46 616 high-resolution remote sensing images. *Photogramm Eng Remote Sens*, 83: 567–579
- 47 617 Liu C, Huang X, Wen D, Chen H, Gong J. 2017. Assessing the quality of building height extraction
48 618 from ZiYuan-3 multi-view imagery. *Remote Sens Lett*, 8: 907–916

- 1
2
3 619 Liu C, Huang X, Zhu Z, Chen H, Tang X, Gong J. 2019. Automatic extraction of built-up area from
4 620 ZY3 multi-view satellite imagery: Analysis of 45 global cities. *Remote Sens Environ*, 226: 51-73
5
6 621 Liu H, Huang X, Wen D, Li J. 2017. The use of landscape metrics and transfer learning to explore
7 622 urban villages in China. *Remote Sens*, 9: 365
8
9 623 Liu X, Hu G, Chen Y, Li X, Xu X, Li S, Pei F, Wang S. 2018. High-resolution multi-temporal mapping
10 624 of global urban land using Landsat images based on the Google Earth Engine Platform. *Remote*
11 625 *Sens Environ*, 209: 227-239
12
13 626 Longbotham N, Chaapel C, Bleiler L, Padwick C, Emery W J, Pacifici F. 2012. Very high resolution
14 627 multiangle urban classification analysis. *IEEE Trans Geosci Remote Sensing*, 50: 1155-1170
15
16 628 Ma Y, Wu H, Wang L, Huang B, Ranjan R, Zomaya A, Jie W. 2015. Remote sensing Big Data
17 629 computing: challenges and opportunities. *Futur Gener Comp Syst*, 51: 47-60
18
19 630 Mallat S G. 1989. A theory for multiresolution signal decomposition: the wavelet representation. *IEEE*
20 631 *Trans Pattern Anal Mach Intell*, 11: 674-693
21
22 632 Marin C, Bovolo F, Bruzzone L. 2015. Building change detection in multitemporal very high resolution
23 633 SAR images. *IEEE Trans Geosci Remote Sensing*, 53: 2664-2682
24
25 634 Marmanis D, Datcu M, Esch T, Stilla U. 2016. Deep learning earth observation classification using
26 635 ImageNet pretrained networks. *IEEE Geosci Remote Sens Lett*, 13: 105-109
27
28 636 Myint S W, Gober P, Brazel A, Grossman-Clarke S, Weng Q. 2011. Per-pixel vs. object-based
29 637 classification of urban land cover extraction using high spatial resolution imagery. *Remote Sens*
30 638 *Environ*, 115: 1145-1161
31
32 639 Musci M, Feitosa R Q, Costa G A O P, Velloso M L F. 2013. Assessment of binary coding techniques
33 640 for texture characterization in remote sensing imagery. *IEEE Geosci Remote Sens Lett*, 10:
34 641 1607-1611
35
36 642 Myint S W, Lam N S N, Tyler J M. 2004. Wavelets for urban spatial feature discrimination.
37 643 *Photogramm Eng Remote Sens*, 70: 803-812
38
39 644 Nogueira K, Penatti O, Santos J. 2017. Towards better exploiting convolutional neural networks for
40 645 remote sensing scene classification. *Pattern Recognit*, 61: 539-556
41
42 646 Ojala T, Pietikäinen M, Harwood D. 1996. A comparative study of texture measures with classification
43 647 based on featured distributions. *Pattern Recognit*, 29: 51-59
44
45 648 Ojala T, Pietikainen M, Maenpaa T. 2002. Multiresolution gray-scale and rotation invariant texture
46 649 classification with local binary patterns. *IEEE Trans Pattern Anal Mach Intell*, 24: 971-987
47
48 650 Ok A O. 2013. Automated detection of buildings from single VHR multispectral images using shadow
49 651 information and graph cuts. *ISPRS-J Photogramm Remote Sens*, 86: 21-40
50
51 652 Ok A O, Senaras C, Yuksel B. 2013. Automated detection of arbitrarily shaped buildings in complex
52 653 environments from monocular VHR optical satellite imagery. *IEEE Trans Geosci Remote Sensing*,
53 654 51: 1701-1717
54
55 655 Ouma Y O, Ngigi T, Tateishi R. 2006. On the optimization and selection of wavelet texture for feature
56 656 extraction from high-resolution satellite imagery with application towards urban-tree delineation.
57 657 *Int J Remote Sens*, 27: 73-104
58
59 658 Pacifici F, Chini M, Emery W J. 2009. A neural network approach using multi-scale textural metrics
60 659 from very high-resolution panchromatic imagery for urban land-use classification. *Remote Sens*
61 660 *Environ*, 113: 1276-1292
62
63 661 Pacifici F, Del Frate F. 2010. Automatic change detection in very high resolution images with
64 662 pulse-coupled neural networks. *IEEE Geosci Remote Sens Lett*, 7: 58-62

- 1
2
3 663 Peng F, Gong J, Wang L, Wu H, Liu P. 2017. A new stereo pair disparity index (SPDI) for detecting
4 664 built-up areas from high-resolution stereo imagery. *Remote Sens*, 9: 633
- 5 665 Peng F, Wang L, Gong J, Wu H. 2015. Development of a framework for stereo image retrieval with
6 666 both height and planar features. *IEEE J Sel Top Appl Earth Observ Remote Sens*, 8: 800-815
- 7
8 667 Pesaresi M, Benediktsson J A. 2001. A new approach for the morphological segmentation of
9 668 high-resolution satellite imagery. *IEEE Trans Geosci Remote Sensing*, 39: 309-320
- 10 669 Pesaresi M, Ehrlich D, Florczyk A, Freire S, Julea A, Kemper T, Soille P, Syrris V. 2015. GHS
11 670 Built-up Grid, Derived from Landsat, Multitemporal (1975, 1990, 2000, 2014). European
12 671 Commission, Joint Research Centre (JRC)
- 13 672 Pesaresi M, Ehrlich D, Caravaggi I, Kauffmann M, Louvrier C. 2011. Toward global automatic
14 673 built-up area recognition using optical VHR imagery. *IEEE J Sel Top Appl Earth Observ Remote*
15 674 *Sens*, 4: 923-934
- 16 675 Pesaresi M, Gerhardinger A. 2011. Improved textural built-up presence index for automatic recognition
17 676 of human settlements in arid regions with scattered vegetation. *IEEE J Sel Top Appl Earth Observ*
18 677 *Remote Sens*, 4: 16-26
- 19 678 Pesaresi M, Gerhardinger A, Kayitakire F. 2008. A robust built-up area presence index by anisotropic
20 679 rotation-invariant textural measure. *IEEE J Sel Top Appl Earth Observ Remote Sens*, 1: 180-192
- 21 680 Pesaresi M, Guo H, Blaes X, Ehrlich D, Ferri S, Gueguen L, Halkia M, Kauffmann M, Kemper T, Lu
22 681 L, Marin-Herrera M A, Ouzounis G K, Scavazon M, Soille P, Syrris V, Zanchetta L. 2013. A
23 682 global human settlement layer from optical HR/VHR RS data: concept and first results. *IEEE J Sel*
24 683 *Top Appl Earth Observ Remote Sens*, 6: 2102-2131
- 25 684 Poullis C. 2014. Tensor-Cuts: A simultaneous multi-type feature extractor and classifier and its
26 685 application to road extraction from satellite images. *ISPRS-J Photogramm Remote Sens*, 95: 93-108
- 27 686 Puissant A, Hirsch J, Weber C. 2005. The utility of texture analysis to improve per-pixel classification
28 687 for high to very high spatial resolution imagery. *Int J Remote Sens*, 26: 733-745
- 29 688 Qian Y, Ye M, Zhou J. 2013. Hyperspectral image classification based on structured sparse logistic
30 689 regression and three-dimensional wavelet texture features. *IEEE Trans Geosci Remote Sensing*, 51:
31 690 2276-2291
- 32 691 Qian Y, Zhou W, Yan J, Li W, Han L. 2015. Comparing machine learning classifiers for object-based
33 692 land cover classification using very high resolution imagery. *Remote Sens*, 7: 153-168
- 34 693 Qin R. 2014. Change detection on LOD 2 building models with very high resolution spaceborne stereo
35 694 imagery. *ISPRS-J Photogramm Remote Sens*, 96: 179-192
- 36 695 Qin R, Fang W. 2014. A hierarchical building detection method for very high resolution remotely
37 696 sensed images combined with DSM using graph cut optimization. *Photogramm Eng Remote Sens*,
38 697 80: 873-883
- 39 698 Reichstein M, Camps-Valls G, Stevens B, Jung M, Denzler J, Carvalhais N, Prabhat. 2019. Deep
40 699 learning and process understanding for data-driven Earth system science. *Nature*, 566: 195-204
- 41 700 Schneider A, Friedl M A, Potere D. 2010. Mapping global urban areas using MODIS 500-m data: New
42 701 methods and datasets based on 'urban ecoregions'. *Remote Sens Environ*, 114: 1733-1746
- 43 702 Sghaier M O, Lepage R. 2016. Road extraction from very high resolution remote sensing optical
44 703 images based on texture analysis and beamlet transform. *IEEE J Sel Top Appl Earth Observ*
45 704 *Remote Sens*, 9: 1946-1958
- 46 705 Shanmugam L, Kaliaperumal V. 2015. Water flow based geometric active deformable model for road
47 706 network. *ISPRS-J Photogramm Remote Sens*, 102: 140-147

- 1
2
3 707 Shao Z, Fu H, Fu P, Yin L. 2016. Mapping urban impervious surface by fusing optical and SAR data at
4 708 the decision level. *Remote Sens*, 8: 945-966
- 5
6 709 Shi X L, Nie S P, Ju W M, Yu L. 2016. Climate effects of the Globe Land30 land cover dataset on the
7 710 Beijing Climate Center climate model simulations. *Sci China Earth Sci*, 59: 1754-1764
- 8
9 711 Song C, Yang F, Li P. 2010. Rotation invariant texture measured by local binary pattern for remote
10 712 sensing image classification. 2010 Second International Workshop on Education Technology and
11 713 Computer Science. 3: 3-6
- 12
13 714 Stewart I D, Oke T R. 2012. Local climate zones for urban temperature studies. *Bull Amer Meteorol*
14 715 *Soc*, 93: 1879-1900
- 15
16 716 Su W, Li J, Chen Y, Liu Z, Zhang J, Low T M, Suppiah I, Hashim S A M. 2008. Textural and local
17 717 spatial statistics for the object-oriented classification of urban areas using high resolution imagery.
18 718 *Int J Remote Sens*, 29: 3105-3117
- 19
20 719 Sun J, Zhang Y, Wu Z, Zhu Y, Yin X, Ding Z, Wei Z, Plaza J, Plaza A. 2019. An efficient and scalable
21 720 framework for processing remotely sensed big data in cloud computing environments. *IEEE IEEE*
22 721 *Trans Geosci Remote Sensing*, 57: 4294-4308
- 23
24 722 Tian J, Chen D M. 2007. Optimization in multi-scale segmentation of high-resolution satellite images
25 723 for artificial feature recognition. *Int J Remote Sens*, 28: 4625-4644
- 26
27 724 Tian J, Cui S, Reinartz P. 2014. Building change detection based on satellite stereo imagery and digital
28 725 surface models. *IEEE Trans Geosci Remote Sensing*, 52: 406-417
- 29
30 726 Tuia D, Pacifici F, Kanevski M, Emery W J. 2009. Classification of very high spatial resolution
31 727 imagery using mathematical morphology and support vector machines. *IEEE Trans Geosci Remote*
32 728 *Sensing*, 47: 3866-3879
- 33
34 729 United Nations. 2018. 2018 Revision of World Urbanization Prospects. Population Division,
35 730 Department of Economic and Social Affairs: United Nations Publications
- 36
37 731 Volpi M, Tuia D, Bovolo F, Kanevski M, Bruzzone L. 2013. Supervised change detection in VHR
38 732 images using contextual information and support vector machines. *Int J Appl Earth Observ Geoinf*,
39 733 20:77-85
- 40
41 734 Voltersen M, Berger C, Hese S, Schmullius C. 2014. Object-based land cover mapping and
42 735 comprehensive feature calculation for an automated derivation of urban structure types at block
43 736 level. *Remote Sens Environ*, 154: 192-201
- 44
45 737 Wang C, Middel A, Myint S W, Kaplan S, Brazel A J, Lukasczyk J. 2018. Assessing local climate
46 738 zones in arid cities: The case of Phoenix, Arizona and Las Vegas, Nevada. *ISPRS-J Photogramm*
47 739 *Remote Sens*, 141: 59-71
- 48
49 740 Wen D, Huang X, Liu H, Liao W, Zhang L. 2017. Semantic classification of urban trees using very
50 741 high resolution satellite imagery. *IEEE J Sel Top Appl Earth Observ Remote Sens*, 10: 1413-1424
- 51
52 742 Wen D, Huang X, Zhang L, Benediktsson J A. 2016. A novel automatic change detection method for
53 743 urban high-resolution remotely sensed imagery based on multiindex scene representation. *IEEE*
54 744 *Trans Geosci Remote Sensing*, 54: 609-625
- 55
56 745 Weng Q. 2012. Remote sensing of impervious surfaces in the urban areas: Requirements, methods, and
57 746 trends. *Remote Sens Environ*, 117: 34-49
- 58
59 747 Xie C, Huang X, Zeng W, Fang X. 2016. A novel water index for urban high-resolution eight-band
60 748 WorldView-2 imagery. *Int J Digit Earth*, 9: 925-941
- 749 Yoo H Y, Lee K, Kwon B D. 2009. Quantitative indices based on 3D discrete wavelet transform for
750 750 urban complexity estimation using remotely sensed imagery. *Int J Remote Sens*, 30: 6219-6239

- 1
2
3 751 Yu X, Zhang B Q, Li Q, Chen J. 2016. A method characterizing urban expansion based on land cover
4 752 map at 30 m resolution. *Sci China Earth Sci*, 59: 1738-1744
- 5
6 753 Zhang C, Sargent I, Pan X, Li H, Gardiner A, Hare J, Atkinson P M. 2019. Joint Deep Learning for
7 754 land cover and land use classification. *Remote Sens Environ*, 221: 173–187
- 8
9 755 Zhang L, Huang X, Huang B, Li P. 2006. A pixel shape index coupled with spectral information for
10 756 classification of high spatial resolution remotely sensed imagery. *IEEE Trans Geosci Remote*
11 757 *Sensing*, 44: 2950-2961
- 12
13 758 Zhang L, Zhang L, Tao D, Huang X. 2013. A modified stochastic neighbor embedding for
14 759 multi-feature dimension reduction of remote sensing images. *ISPRS-J Photogramm Remote Sens*,
15 760 83: 30-39
- 16
17 761 Zhang T, Huang X. 2018. Monitoring of urban impervious surfaces using time series of high-resolution
18 762 remote sensing images in rapidly urbanized areas: A case study of Shenzhen. *IEEE J Sel Top Appl*
19 763 *Earth Observ Remote Sens*, 11: 2692-2708
- 20
21 764 Zhang T, Huang X, Wen D, Li J. 2017. Urban building density estimation from high-resolution
22 765 imagery using multiple features and support vector regression. *IEEE J Sel Top Appl Earth Observ*
23 766 *Remote Sens* 10: 3265-3280
- 24
25 767 Zhang X, Du S. 2015. A Linear Dirichlet Mixture Model for decomposing scenes: Application to
26 768 analyzing urban functional zonings. *Remote Sens Environ*, 169: 37-49
- 27
28 769 Zhang Y, Zhang H, Lin H. 2014. Improving the impervious surface estimation with combined use of
29 770 optical and SAR remote sensing images. *Remote Sens Environ*, 141: 155-167
- 30
31 771 Zhou P, Cheng G, Liu Z, Bu S, Hu X. 2016. Weakly supervised target detection in remote sensing
32 772 images based on transferred deep features and negative bootstrapping. *Multidimens Syst Signal*
33 773 *Process*, 27: 925–944
- 34
35 774 Zhu X X, Tuia D, Mou L, Xia G S, Zhang L, Xu F, Fraundorfer F. 2017. Deep learning in remote
36 775 sensing: A comprehensive review and list of resources. *IEEE Geosci Remote Sens Mag*, 5(4):8-36
37
38
39
40
41
42
43
44
45
46
47
48
49
50
51
52
53
54
55
56
57
58
59
60